

This article appeared in a journal published by Elsevier. The attached copy is furnished to the author for internal non-commercial research and education use, including for instruction at the authors institution and sharing with colleagues.

Other uses, including reproduction and distribution, or selling or licensing copies, or posting to personal, institutional or third party websites are prohibited.

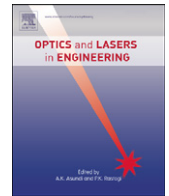
In most cases authors are permitted to post their version of the article (e.g. in Word or Tex form) to their personal website or institutional repository. Authors requiring further information regarding Elsevier's archiving and manuscript policies are encouraged to visit:

<http://www.elsevier.com/copyright>



Contents lists available at ScienceDirect

## Optics and Lasers in Engineering

journal homepage: [www.elsevier.com/locate/optlaseng](http://www.elsevier.com/locate/optlaseng)

## Processing discontinuous displacement fields by a spatio-temporal derivative technique

A.M.R. Sousa<sup>a,\*</sup>, J. Xavier<sup>a</sup>, J.J.L. Morais<sup>a</sup>, V.M.J. Filipe<sup>b</sup>, M. Vaz<sup>c</sup><sup>a</sup> CITAB, University of Trás-os-Montes and Alto Douro, Engenharias I, 5001-801 Vila Real, Portugal<sup>b</sup> CIDESD, University of Trás-os-Montes and Alto Douro, 5001-801 Vila Real, Portugal<sup>c</sup> Faculty of Engineering, University of Porto, Porto, Portugal.

## ARTICLE INFO

## Article history:

Received 4 April 2011

Received in revised form

13 July 2011

Accepted 13 July 2011

Available online 27 July 2011

## Keywords:

Digital image correlation

Spatio-temporal derivatives

Discontinuous displacement fields

## ABSTRACT

In this paper, a digital image correlation (DIC) method coupling cross-correlation with spatio-temporal differential techniques was proposed for assessing discontinuous displacement fields. The accuracy and robustness of the algorithm was assessed on a set of numerical tests by processing computer generated speckled-pattern images. Fracture mechanical tests in mode I were considered, in which both in-plane and out-of-plane rigid-body movements were taken into account. The ability for recovering the analytical asymptotic displacement field in mode I was analysed, and stress intensity factor, crack opening displacement and crack tip location were used as quantitative parameters for validation purposes. Throughout these tests, the results obtained with the proposed method were systematically compared to the ones from Aramis DIC-2D commercial code. Globally, the results computed from both methods are in good agreement with reference values. However, due to the high spatial resolution (point-wise characteristic), a better matching of the displacements in the neighbourhood of discontinuities could be obtained by the proposed method.

© 2011 Elsevier Ltd. All rights reserved.

## 1. Introduction

In the last decades full-field optical techniques of displacement or strain measurement have become widespread tools in experimental solid mechanics [1]. In contrast with conventional strain gauges or extensometers, these techniques are contact-free and provide full-field measurements over a spectrum of different length scales. Based on the nature of the physical phenomenon involved, these techniques can be classified into interferometric (e.g., speckle and moiré interferometry or shearography) and white-light (e.g., digital image correlation and grid or moiré methods). Interferometric techniques are based on the interference of light waves and have typically high sensitivity and resolution. However, they rely on specific and expensive equipment such as lasers (monochromatic and coherent light source) and anti-vibration tables. On the other hand, white-light techniques are based on the spatial variation of light intensity reflected over a textured pattern, which can be either random (image correlation techniques) or periodic (phase-measuring techniques). This pattern can exist naturally on the material surface of interest or can be created by some suitable procedure (i.e., by

painting or bonding). This class of techniques has the advantage of requiring simpler experimental set-ups than interferometry counterparts, and therefore they can be more easily coupled with conventional apparatus such as universal mechanical testing machines.

Among these techniques, DIC has been receiving much attention because of its relatively simple principle and flexibility in terms of its adjustable resolution [2,3]. In order to overcome the discrete feature of digital images, improvements have been achieved, since early stages of the method, in sub-pixel algorithms to enhance the measurements sensitivity and accuracy [4–6]. The quantification of measuring errors by DIC methods have been also addressed from both numerical [7] and experimental [8,9] points of view. However, despite the improvement of pixel resolution of digital cameras (hardware), an inherent limitation of the classical DIC method is the subset-based calculation, which pixel size parameter is most often chosen in a compromise between accuracy (improved with large sub-windows) and interpolation (improved by small sub-windows) errors. In this context, several studies have addressed the optimisation of the subset size with regard to spectral properties of the textured pattern characterising the material surface under investigation [10–14]. Besides, the classical DIC method is most suitable for measuring continuous displacement fields. Therefore, when in presence of discontinuous displacement fields – such as in fracture mechanical studies – the measurements provided by DIC in the neighbourhood of the

\* Correspondence to: CITAB, University of Trás-os-Montes and Alto Douro, Engenharias I, Apartado 1013, 5001-801 Vila Real, Portugal. Tel.: +351 259 350 000; fax: +351 259 350 480.

E-mail address: [amrs@utad.pt](mailto:amrs@utad.pt) (A.M.R. Sousa).

discontinuity region may be inaccurate. Thus, more recently, novel approaches have been developed to enhance the spatial resolution of the method, in order to be able to deal with discontinuous kinematic fields [15–19]. Jin and Bruck [15] coupled the DIC method with the optimisation using genetic algorithm in order to evaluate displacements at each pixel within a subset, with sub-pixel accuracy. Both numerical tests on computer-generated sinusoidal images and experimental tests were performed to validate the proposed method. This piecewise approach allows for fine spatial resolution but it is time consuming and, moreover, can be sensitive to the initial guess and domain of design variables setting on the genetic algorithm code. Another approach has been proposed by Réthoré et al. [16,17], the so-called extended digital image correlation (X-DIC). In this method, the domain of the image is discretised by finite elements. The nodal displacements are then determined by globally correlate reference and mapped deformed images. Using suitable element shape functions, this method can be applied to crack identification in problems of fracture mechanics. In order to improve this calculation method, Chen et al. [18] have proposed a two-step X-DIC algorithm allowing error minimisation in computing discontinuous full-field displacements with large rigid-body translation component. The reliability of the method was verified experimentally through a set of rigid-body and mechanical tests. Poissant and Barthelat [19] have proposed a new algorithm to deal with discontinuous displacement fields. In this method, a given subset is allowed to split into two new correlation regions in the presence of a discontinuity. The robustness of the method was verified on a set of numerical and experimental mode I and mode II fracture mechanical tests. In practice, however, one limitation of this approach can be the size of the split subsets, which pixel dimension should be defined with regard to the speckled pattern to ensure accuracy and isotropy in the subset matching process [2].

The authors [18] have proposed a method to measure the displacements fields on the surface of planar objects with sub-pixel resolution, by combining image correlation with a differential technique. In this method, a coarse approximation of the displacements at pixel level is firstly obtained by cross-correlation, and then a fine approximation to assess sub-pixel displacements is determined by means of an optical flow method based on a differential technique. This approach was validated on a set of numerical tests, which consisted in rigid-body translation and rotation tests, as well as tensile and shear mechanical tests [18]. In the present work, the goal was to extend the application of this point-wise digital image correlation algorithm for measuring discontinuous displacement fields. The accuracy and robustness of the method were assessed on a set of numerical tests by processing synthetic speckled-pattern images. In the framework of linear elastic fracture mechanics, numerical tests under opening mode I, neglecting and including in-plane and out-of-plane rigid-body movements, were analysed. The results obtained from the proposed method were systematically compared to references as well as to data obtained with GOM<sup>®</sup> Aramis v6.0.2 DIC2D commercial code.

## 2. The proposed digital image correlation method

The proposed digital image correlation method consists on a two steps coarse-fine approach: pixel level (coarse) estimation and sub-pixel level (fine) estimation of displacement fields. In the first step, the normalised cross-correlation is recursively applied over the sub-images obtained from the original images pair, using a quad-tree splitting process. In the second step, an optical flow method based on a differential technique is used. A flowchart representation with an overview of the proposed method is presented in Fig. 1.

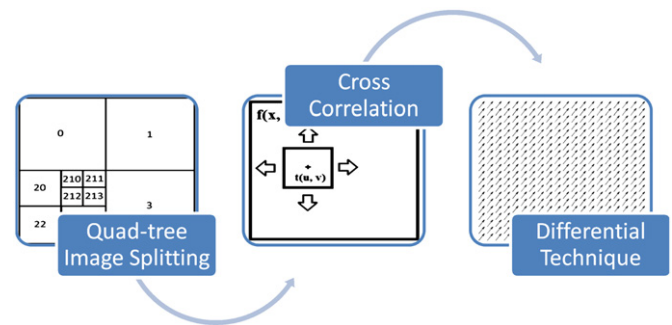


Fig. 1. Overview flowchart representation of the proposed method.

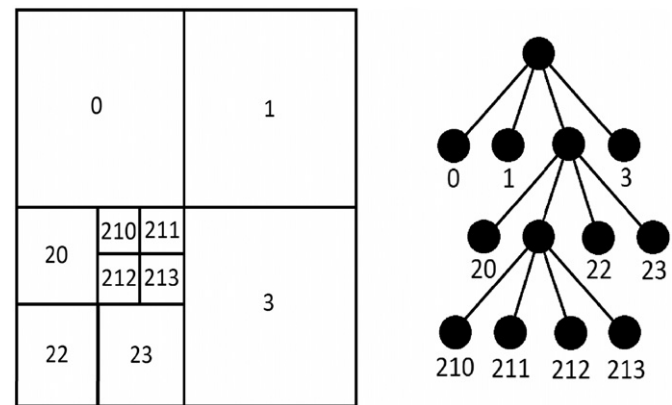


Fig. 2. Quad-tree image splitting process.

### 2.1. Pixel level estimation

The pixel level displacement estimation is performed over a pair of images obtained before (reference) and after surface deformation (deformed). Using a quad-tree process each image is divided into a set of sub-images and the normalised cross-correlation [21,22] is applied to obtain the displacement of each sub-image centre points.

The image splitting (see Fig. 2) is similar to a quad-tree division process and is used to enable pixel level displacements estimation between reference and deformed images, following a global to local approach. Firstly, a global displacement between full sized images is calculated using the correlation coefficient. Secondly, both images (reference and deformed) are submitted to the splitting process using a quad-tree technique, which consists in dividing each image recursively into four sub-images and repeating for each pair the normalised cross-correlation. This procedure is repeated recursively until the pre-defined criteria [20] are fulfilled. Finally, at the end of the splitting process, a coarse map of pixel level displacements between reference and deformed image is obtained.

### 2.2. Sub-pixel level estimation

After finding a pixel level displacement between the two images, sub-pixel estimation is applied to obtain higher resolution. Each reference sub-image (resulting from the quad-tree decomposition) is shifted by their amount of pixel level displacement over the correspondent deformed sub-image. Next, the displacement estimation of each pixel belonging to the sub-image is computed using a differential technique. The main stages of this processing consist of the following: (1) prefiltering or smoothing with low-pass/band-pass filters to extract signal structure of interest and enhance signal-to-noise ratio; (2) extraction of basic measurements

such as spatio-temporal derivatives (to measure the components of velocity) and (3) integration of the previously extracted measurements to produce a smooth 2D flow field. The method implements a first-order derivative technique, more specifically, the local differential technique from Lucas and Kanade [23]. This technique implements a weighted least-squares (LS) fit of local first-order constraints to a constant model  $v$  in each small spatial neighbourhood  $\Omega$  of position  $\chi=(x,y)$ , by minimising

$$\sum_{\chi \in \Omega} W^2(\chi) [\nabla I(\chi, t) v + I_t(\chi, t)]^2 \quad (1)$$

A weighting function  $W(\chi)$  is used in order to give more influence to constraints at the centre of the neighbourhood than at the periphery. Depending on the speckle size, this function could be adjusted in order to control the spatial resolution (i.e., the windows size). Gaussian functions are usually used for this purpose; however, other functions or weighting schemes can be used.  $\nabla I(\chi, t)$  is the spatial intensity gradient,  $\mathbf{v}=(v_x, v_y)$  represents the two components image velocity and  $I_t(\chi, t)$  is the partial time derivative of image intensity at position  $\chi$  in instant  $t$ . The displacement field resulting from differential technique has sub-pixel resolution.

### 2.3. Full displacement estimation

The global displacement of each pixel is then obtained by adding its coarse pixel level displacement (cross-correlation) with the respective finer sub-pixel level displacement (differential technique).

## 3. Numerical test methods

Numerical tests were carried out on computer generated speckled-pattern images in order to assess the accuracy and efficiency of the proposed DIC method when dealing with discontinuous displacement fields. These discontinuous fields can occur, for instance, in fracture mechanical tests. Linear elastic fracture mechanics (LEFM) was assumed herein. According to this theory, the nonlinear material events occurring near the crack tip are supposed confined to a very small region, which is an order of magnitude inferior to the crack size or other characteristic dimensions of the body. Under this assumption, the state of stress in the neighbourhood of the crack tip can be characterised by  $K$ , the stress intensity factor (unit:  $\text{Pa}\sqrt{\text{m}}$ ). There are three elementary crack propagation modes: (a) opening mode or mode I; (b) sliding mode or mode II and (c) tearing mode or mode III. A schematic representation of fracture in mode I is shown in Fig. 3, where  $P$  is the applied load,  $\delta$  is the relative displacement of its points of application and  $a(P)$  represents the crack length during propagation. For the sake of validation, numerical tests based on the analytical asymptotic displacement field in mode I were investigated in this work. For quantitative evaluation of the measured displacement fields, stress intensity factor ( $K_I$ ), crack opening displacement and crack tip location were further analysed. Effects of in-plane and out-of-plane rigid-body movements (which can occur in experimental tests) were also taken into account. In all the case studies, the results obtained with the proposed method were compared and discussed with regard to the ones provided by GOM<sup>®</sup> Aramis v6.0.2 DIC 2D commercial software [24], when processing the same set of images. Considering the typical speckled-pattern images (Section 3.1), the size of the correlation window used in the proposed method was  $19 \times 19$  pixels, whilst the subset on the Aramis was defined as  $15 \times 15$  pixels (with a step size of  $15 \times 15$  pixels).

### 3.1. Synthetic speckled-pattern images

The images to be processed by digital image correlation were numerically generated on the computer. In order to obtain a pair

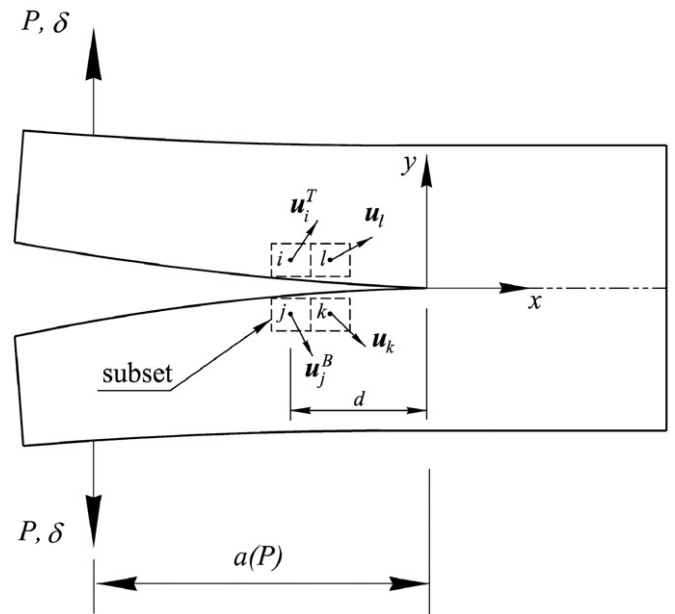


Fig. 3. Elementary crack propagation in mode I.

of images, corresponding to different configurations, before and after a given applied deformation, an analytical function was chosen for deforming a reference speckled-pattern image according to the following expression:

$$I(x, y) = \sum_{i=0}^{N_s} I_i^0 \exp \left\{ -\frac{[x-x_k-U(x, y)]^2 + [y-y_k-V(x, y)]^2}{R^2} \right\} \quad (2)$$

$(x, y)$  are the pixel coordinates on the image,  $I_i^0 \in [0, 255]$  (image of 8 bits) represent a random background light intensity value,  $R$  and  $N_s$  define the size and number of the speckle marks on the pattern, respectively, and  $U(x, y)$  and  $V(x, y)$  are the applied displacement field components.

To start with, a black  $H(\text{width}) \times V(\text{height})$  image with a depth of 8 bits was initialised. A reference image (undeformed configuration:  $U(x, y)=V(x, y)=0$  in Eq. (2)) can be generated by iteratively superimposing images characterised by a single Gaussian distribution spot with radius  $R$ . The total number of speckles ( $N_s$ ) as well as their central location  $(x_k, y_k)$  within the spatial domain of the image were randomly chosen, in order to obtain a stochastic speckled pattern suitable for digital image correlation. A deformed image can then be generated with regard to this reference image by applying an inverse displacement field (Eq. (2)). Finally, a  $5 \times 5$  Gaussian filter was applied to the images, in order to obtain a smooth speckled-pattern texture. A typical image generated from Eq. (2) is shown in Fig. 4a ( $H=V=1000$  pixels,  $N_s=6667$ ,  $R=5$  pixels).

### 3.2. Mode I fracture mechanical test

#### 3.2.1. Asymptotic displacement field

**3.2.1.1. Neglecting rigid-body movements.** The analytical mode I asymptotic displacement field can be given by [25]

$$U_I(r, \theta) = \frac{K_I}{2E} \sqrt{\frac{r}{2\pi}} (1 + \nu) \left[ (2k-1) \cos \frac{\theta}{2} - \cos \frac{3\theta}{2} \right] \quad (3.1)$$

$$V_I(r, \theta) = \frac{K_I}{2E} \sqrt{\frac{r}{2\pi}} (1 + \nu) \left[ (2k+1) \sin \frac{\theta}{2} - \sin \frac{3\theta}{2} \right] \quad (3.2)$$

where  $(r, \theta)$  are polar coordinates centred on the crack tip,  $K_I$  is the stress intensity factor in mode I,  $E$  and  $\nu$  are modulus of elasticity and Poisson's ratio, respectively, and  $k=3-4\nu$  for plane strain.



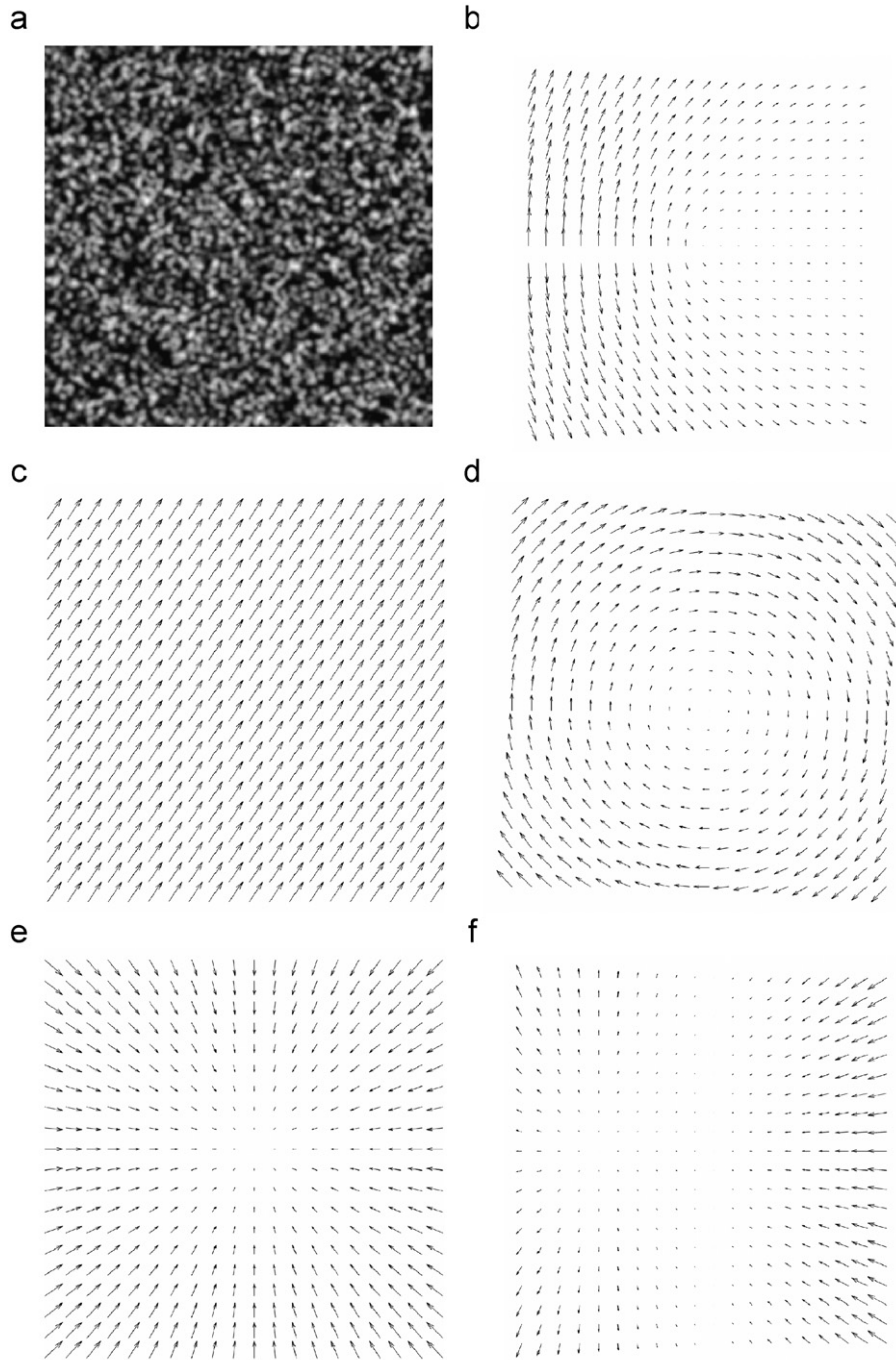


**Fig. 4.** (a) Computer generated speckled-pattern image (8 bit image); (b) opening mode I reference displacement field (material: polymer epoxy;  $E=2.8$  GPa,  $\nu=0.47$ ,  $K_I=300\text{MPa}\sqrt{\text{pixel}}$ ). (c) in-plane translation ( $U_0=0.8$  pixel,  $V_0=1.2$  pixel); (d) in-plane rotation—origin at the centre of the image ( $\theta=-0.18$  degrees); (e) out-of-plane translation ( $\Delta Z=-0.8$  mm); (f) out-of-plane rotation about the Y direction of the image of 2 degrees (corresponding to a maximum  $\Delta Z$  of  $-0.8$  mm).

The displacement field in Eqs. (3) is shown in Fig. 4b, considering a spatial domain of  $1000 \times 1000$  pixels and a horizontal crack length with the tip located at the centre of the image. In this study, a polymer epoxy material with elastic properties of  $E=2.8$  GPa and  $\nu=0.47$  was selected. Moreover, a stress intensity factor of  $K_I=300\text{MPa}\sqrt{\text{pixel}}$  was chosen.

**3.2.1.2. Including in-plane rigid-body movements.** Normally, the experimental displacement of a deformed object includes rigid-body movements in the plane of the object; this can involve both

translation and rotation movements. The in-plane translation is simply given by

$$U_T^{\text{in}}(x,y) = U_0 \quad (4.1)$$

$$V_T^{\text{in}}(x,y) = V_0 \quad (4.2)$$

where  $U_0$  and  $V_0$  are constants quantifying the applied displacement, respectively, along the X and Y directions across the image. Fig. 4c illustrates a given translation displacement field (Eqs. 4), in which  $U_0=0.8$  pixel and  $V_0=1.2$  pixel. The in-plane rotation  $\alpha$ , with regard to a given rotation point, generates

displacement fields according to the following relationship (small rotation assumption):

$$U_R^{\text{in}}(x,y) = \alpha y \quad (5.1)$$

$$V_R^{\text{in}}(x,y) = -\alpha x \quad (5.2)$$

where  $(x,y)$  are the coordinates of the image. Fig. 4d shows the in-plane rotation field (Eqs. 5) assuming  $\alpha = -0.18$  degree and the point of rotation at the centre of the image.

**3.2.1.3. Including out-of-plane rigid-body movements.** In a monocular system, the measurement of in-plane displacements is coupled with out-of-plane movements [8]. Assuming a pinhole camera model for image formation, a given out-of-plane displacement  $\Delta Z$  generates in-plane apparent displacements according to

$$U_T^{\text{out}}(x,y) \approx -\frac{L}{Z} X \left( \frac{\Delta Z}{Z} \right) = x \left( \frac{\Delta Z}{Z} \right) \quad (6.1)$$

$$V_T^{\text{out}}(x,y) \approx -\frac{L}{Z} Y \left( \frac{\Delta Z}{Z} \right) = y \left( \frac{\Delta Z}{Z} \right) \quad (6.2)$$

where  $(X,Y)$  are the coordinates of an imaged “point” of the object,  $(x,y)$  are its corresponding projection on the camera sensor,  $L$  is the image distance and  $Z$  is the initial object distance. A hypothetical example was considered here by selecting  $L=60$  mm,  $Z=300$  mm (magnification factor  $M_T = -L/Z = -0.2$  and focal length  $f = (1/L + 1/Z)^{-1} = 50$  mm) and a field of view corresponding to a square region of 20 mm. Moreover, a maximum out-of-plane displacement of  $\Delta Z = -0.8$  mm was assumed. The displacement field (Eqs. 6) generated in this case study is shown in Fig. 4e.

An out-of-plane rotation  $\theta(\Delta Z)$  can also occur experimentally inducing a variation of the out-of-plane movement ( $\Delta Z$ ) across the field of view. For a given clockwise, out-of-plane rotation about the  $Y$  axis, and assuming a first-order approximation, the pinhole camera

model gives the following solution for the coupled in-plane displacement fields:

$$U_R^{\text{out}}(x,y) \approx -\frac{L}{Z} X \left( \cos \theta - 1 + \frac{X \sin \theta \cos \theta}{Z} \right) \quad (7.1)$$

$$V_R^{\text{out}}(x,y) \approx -\frac{L}{Z} Y \left( \frac{X \sin \theta}{Z} \right) \quad (7.2)$$

where  $\Delta Z(x,y) = X \sin \theta$ . A representation of the displacement fields in Eqs. (7) is shown in Fig. 4f assuming an out-of-plane rotation about the  $Y$  direction of 2 degree (which corresponds to a maximum out-of-plane movement of  $\Delta Z = -0.8$  mm).

### 3.2.2. Crack opening displacement

The crack opening displacement (COD) is defined as the distance separating cracked surfaces, measured at a certain distance behind the crack tip, at a given stage. This quantity is usually measured experimentally, together with the applied load generating fracture in mode I and the relative displacement of its points of application. The COD in mode I (COD<sub>I</sub>) can be evaluated from the displacement field components provided by digital image correlation as

$$\text{COD}_I = \|V_j^B - V_i^T\| \quad (8)$$

where  $V \equiv V(x,y)$  is the vertical component of the displacement associated to a pair  $(i,j)$  of correlation windows selected on top ( $T$  in Fig. 3) and bottom ( $B$  in Fig. 3) of the cracked surface.

### 3.2.3. Crack tip location

The crack tip location can be estimated from the displacement fields provided by digital image correlation. A methodology based on the norm of the relative position vector between neighbour points has been proposed in Refs. [26–28]. The algorithm is applied to a given set of four adjacent points  $(i, j, k$  and  $l)$  as illustrated in Fig. 3.

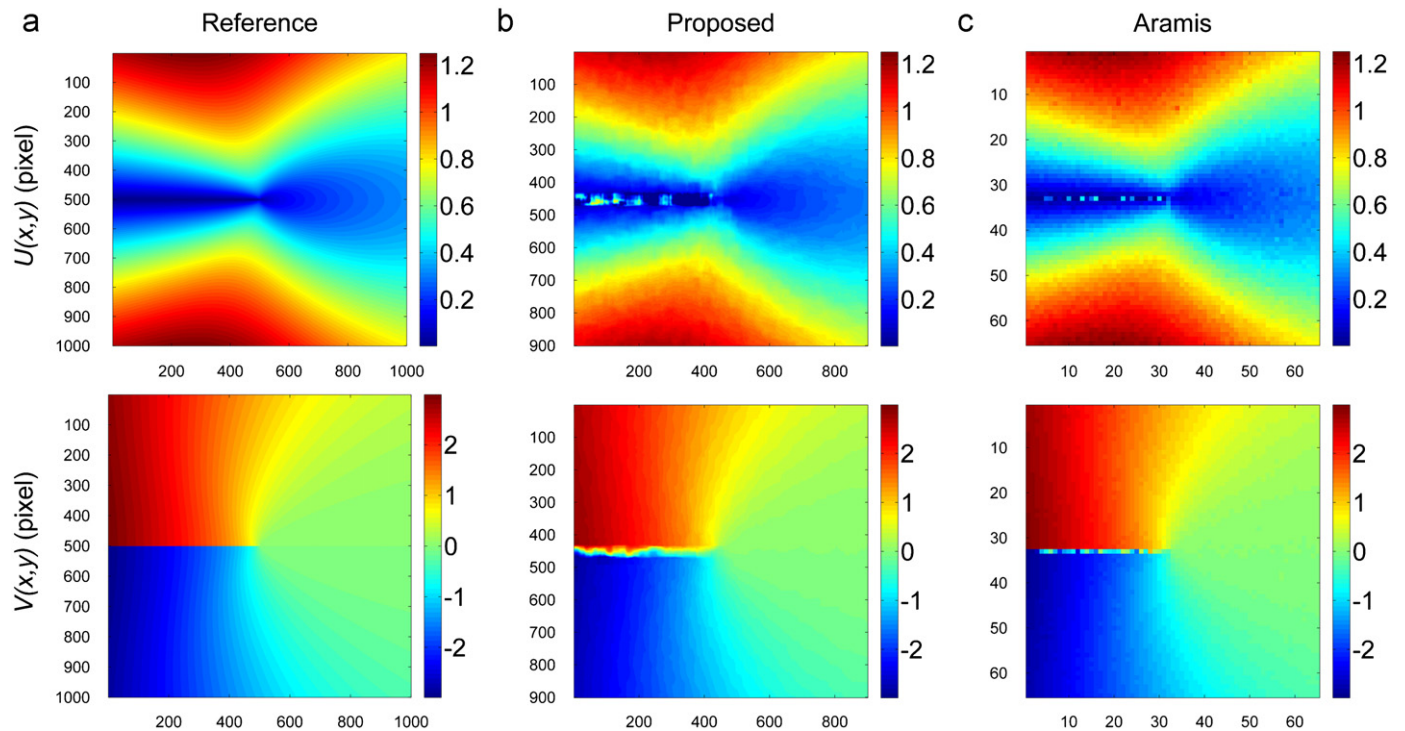


**Fig. 5.** Fracture displacement fields in mode I, neglecting rigid-body movements: (a) reference, calculated by (b) proposed ( $901 \times 901$  pixels) and (c) Aramis ( $65 \times 65$  subsets) DIC methods.

In classical digital image correlation, these points can correspond to the centroids of adjacent subsets through the horizontal and vertical directions of the image. An auxiliary function is then defined as

$$A(x,y) = \max(\|\mathbf{u}_i - \mathbf{u}_k\|; \|\mathbf{u}_j - \mathbf{u}_l\|) \quad (9)$$

where  $\mathbf{u}_p$  is the displacement vector of point  $p$  (with  $p=i,j,k,l$ ). The norm function of the displacements in Eq. (9) represents the relative variation of the distance between pair of points (see Fig. 3). Function  $A(x,y)$  can be evaluated across the entire region of interest. A criterion is then defined according to the following inequalities:

$$\begin{cases} M(x,y) = 1 & \text{if } A(x,y) \geq c\bar{A} \\ M(x,y) = 0 & \text{if } A(x,y) < c\bar{A} \\ M(x,y) = -1 & \text{if } A(x,y) = \text{Not a Number(NaN)} \end{cases} \quad (10)$$

where  $c$  is a constant value and  $\bar{A}$  represents the average of  $A(x,y)$ . This thresholding process allows the definition of a mask  $M(x,y)$

(Eq. (10)) labelling the measuring region according to the following description:

- $M(x,y)=1$  defines the region where a discontinuity is present but the material is not completely damaged. This happens at the crack tip;
- $M(x,y)=0$  corresponds to the region where the material is undamaged;
- $M(x,y)=-1$  represents the region where the material is completely cracked and typically no information is available in the digital image correlation.

### 3.2.4. Stress intensity factor evaluation

According to LEFM, the stress intensity factor in mode I ( $K_I$ ) can be determined directly from the displacement fields measured around the crack tip, providing that the elastic properties of the

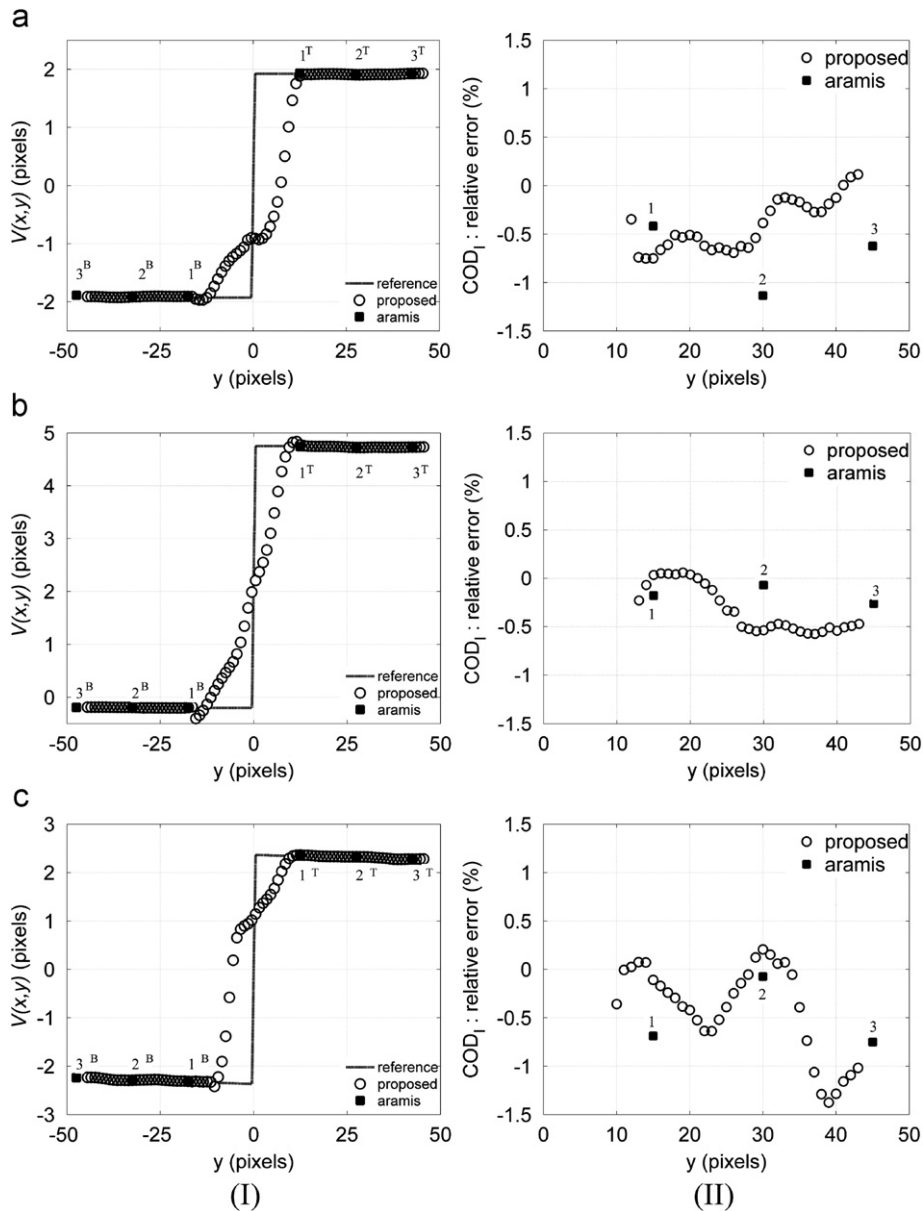


**Fig. 6.** (I)  $V(x,y)$  displacement along a line segment crossing the cracked surface at a distance  $d=208$  pixels behind the crack tip; (II) relative error on the evaluation of  $COD_I$ , in the cases of the following: (a) neglecting, (b) including in-plane and (c) including out-of-plane rigid-body movements.

material are known (Eqs. 3). Field data is provided by digital image correlation, so an overdetermined system of equations is obtained. In order to solve this system of equation for  $K_I$ , a least-squares approach can be used [29,30]. Let us consider the  $U_I(x,y)$  displacement field (Eq. 3.1)

$$U_I(x_i, y_i) = \sqrt{\frac{r_i}{2\pi}} \frac{(1+\nu)}{2E} \left[ (2k-1) \cos \frac{\theta_i}{2} - \cos \frac{3\theta_i}{2} \right] K_I \quad (i = 1, \dots, N) \quad (11.1)$$

or, in matrix form

$$[U_I] = [C_U][X] \quad (11.2)$$

where  $[U_I]_{N \times 1}$  is a vector assembling the  $U_I$  displacements at each measuring point  $(x_i, y_i)$ ,  $[C_U]_{N \times 1}$  is a coefficient matrix depending on the elastic properties of the material and point coordinates,  $[X]_{1 \times 1} = K_I$  is the vector of unknown quantity and  $N$  is the total number of independent measuring points in the field. In order to solve Eqs. (11) the concept of pseudo-inverse matrix is used:

$$[X] = ([C_U]^T [C_U])^{-1} [C_U]^T [U_I] \quad (12)$$

The same approach can be applied to the  $V_I(x,y)$  components of the displacement field (Eq. (3.2)). Finally, the following overdetermined system of equations can be used for evaluating  $K_I$ :

$$[X] = \left( \begin{bmatrix} [C_U]^T \\ [C_V]^T \end{bmatrix}_{1 \times 2N} \begin{bmatrix} [C_U] \\ [C_V] \end{bmatrix}_{2N \times 1} \right)^{-1} \begin{bmatrix} [C_U]^T \\ [C_V]^T \end{bmatrix}_{1 \times 2N} \begin{bmatrix} [U_I] \\ [V_I] \end{bmatrix}_{2N \times 1} \quad (13)$$

Thus, the parameter  $K_I$  is evaluated by approximating in the least-squares sense the calculated displacements to the theoretical ones given by Eqs. (3).

The least-squares approach described above is particularly suitable when determining stress intensity factor from displacement fields incorporating rigid-body movements (Eqs. (4–7)), which are always presented in experimental tests. In this case, the total displacement is defined by adding the displacements associated to each different contribution (superposition principle). As an example, assuming pure mode I fracture ( $U_I$ , from Eq. 3.1) and both in-plane translation ( $U_T^{\text{in}}$ , from Eq. 4.1) and rotation ( $U_R^{\text{in}}$ , from Eq. (5.1)), the measured displacement fields are given by

$$U(x,y) = U_I + U_T^{\text{in}} + U_R^{\text{in}} = [C_U][X] \quad (14.1)$$

with

$$[C_U] = \left[ \sqrt{\frac{r_i}{2\pi}} \frac{(1+\nu)}{2E} \left[ (2k-1) \cos \frac{\theta_i}{2} - \cos \frac{3\theta_i}{2} \right] 1 y_i \right] \quad (14.2)$$

$$[X]^T = [K_I \quad U_0 \quad \alpha]$$

A similar equation can be obtained for the  $V_I(x,y)$  displacement. Thus, the overdetermined system of equations so obtained can be solved in the least-squares sense in order to determine the stress intensity factor by eliminating any possible rigid-body movement. This approach can also be applied to out-of-plane movements by taking into account the corresponding displacement fields (see Appendix A).

## 4. Results and discussion

### 4.1. Mode I fracture mechanical test neglecting rigid-body movements

A pair of synthetic image simulating a pure fracture mechanical test in mode I was created by considering the reference displacement field (Eqs. 3) shown in Fig. 5a. By processing this pair of images, displacements were calculated by both proposed and Aramis DIC methods as shown in Figs. 5b and c, respectively. Generically, both methods qualitatively retrieved the reference displacements (with residual maps, obtained by subtracting the

reference and calculated displacement fields, with amplitude less than 0.2%), although with a different spatial resolution (Fig. 5). Nevertheless, some perturbations were obtained around the crack extension. It is worth noticing that some perturbations in the vicinity of the opened cracked region may also be attributed to the generation of the deformed images itself (blur effects) (Eq. (2)), whose area in this case is mainly defined by the parameter  $K_I$  (by increasing the value of  $K_I$ , a larger opened cracked area is obtained).

The profile of the reference and calculated  $V(x,y)$  displacement component along a line segment crossing the crack surface at a distance  $d=208$  pixels from the crack tip (located at the centre of the image, see Fig. 4b) is shown in Fig. 6a–l. As it can be seen, both methods accurately follow the reference displacement in the neighbourhood of the crack discontinuity. However, since the proposed method has a higher spatial resolution, more data points are obtained for an accurate reconstruction of the displacement profile

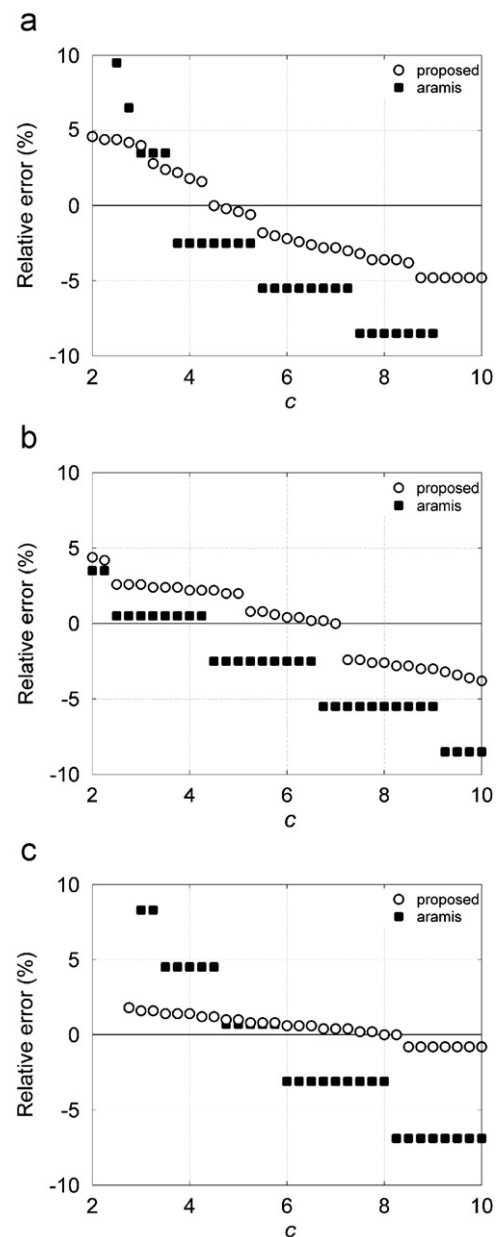


**Fig. 7.** Crack tip location estimated from proposed and aramis DIC methods as a function of the parameter  $c$  (Eq. (10)) in the cases of: (a) neglecting, (b) including in-plane and (c) including out-of-plane rigid-body movements.



in the discontinuity. Fig. 6a-II shows the relative error on measuring  $COD_I$  (Eq. (8)) from both methods with regard to the reference one. This error is typically less than 1%, but it is smaller for the proposed method than Aramis.

Experimentally, the increment of crack length ( $a$  in Fig. 3) during a crack propagation test is usually measured together with the applied load and the displacement of its point of application. Therefore, it is relevant to use digital image correlation for the estimation of the crack tip location. The displacement fields measured from both methods were processed in order to estimate the crack tip location according to the approach described in Section 3.2.4. The reference crack tip is located at the centre of the image:  $H/2 = V/2 = 500$  pixels. The relative error obtained for both methods with regard to the reference location is shown in Fig. 7a, as a function of the parameter  $c \in [3, 6]$  (see Eqs. (10)). This parameter works here as a threshold for classifying the spatial domain of the field data for crack identification. As it can be concluded a more accurate estimation is achieved by the proposed method when compared with the Aramis one, with exact crack location for  $c = 4.5$ .

A least-squares approach was applied in order to solve Eqs. (3) for assessing stress intensity factor  $K_I$  (Section 3.2.4). The parameter  $K_I$  is then evaluated by approximating the calculated displacements to the theoretical ones given in Eqs. (3) in the

least-squares sense. The results obtained from this approach are summarised in Table 1. In order to study the sensitivity of  $K_I$  with regard to the displacement field components, this value was determined in the least-squares sense taken separately  $U(x, y)$  and  $V(x, y)$  displacement fields and finally considering both together ( $U(x, y), V(x, y)$ ). For the proposed method, in all cases,  $K_I$  could be accurately calculated with differences less than 0.5%. This value was also conveniently determined from the displacement fields measured by the Aramis method, although with a slightly high deviation, namely when only using the  $V(x, y)$  displacement field (about 1%).

#### 4.2. Mode I fracture mechanical test including in-plane rigid-body movements

In practice, in-plane translation and rotation rigid-body displacements can be measured together with the deformation of a given object. In applications where deformation fields are to be reconstructed from raw displacement fields provided by digital image correlation, rigid-body movements may not represent an issue since differentiation methods are usually employed. However, when processing directly the displacement fields, rigid-body movements must be taken into account. In order to quantify the influence of in-plane rigid-body movements on processing fracture displacement fields in mode I, a case study is proposed by coupling fracture displacement fields (Eqs. 3) with both translation (Eq. 4) and rotation (Eq. 5) movements.

The resulting displacement fields obtained by superposition of fracture (Fig. 4b) and rigid-body movements (Fig. 4c and d) are shown in Fig. 8. Both proposed and Aramis DIC methods qualitatively follow the reference displacement maps. As in the previous Section 4.1, these displacement fields were further processed in order to calculate  $COD_I$  (Fig. 6b-I). Also in this case, the relative error is less than 1% obtained from both methods with regard to the reference one (Fig. 6b-II).

**Table 1**  
Evaluation of mode I stress intensity factor,  $K_I$ , from displacement fields based on least-squares regression—neglecting rigid-body movements.

	$K_I$ (MPa $\sqrt{\text{pixel}}$ )		
	Reference	Proposed	Aramis
$U$ :	300	300.90 (0.30%)	300.87 (0.29%)
$V$ :	300	298.87 (−0.38%)	296.90 (−1.03%)
$U, V$ :	300	299.17 (−0.28%)	297.68 (−0.77%)

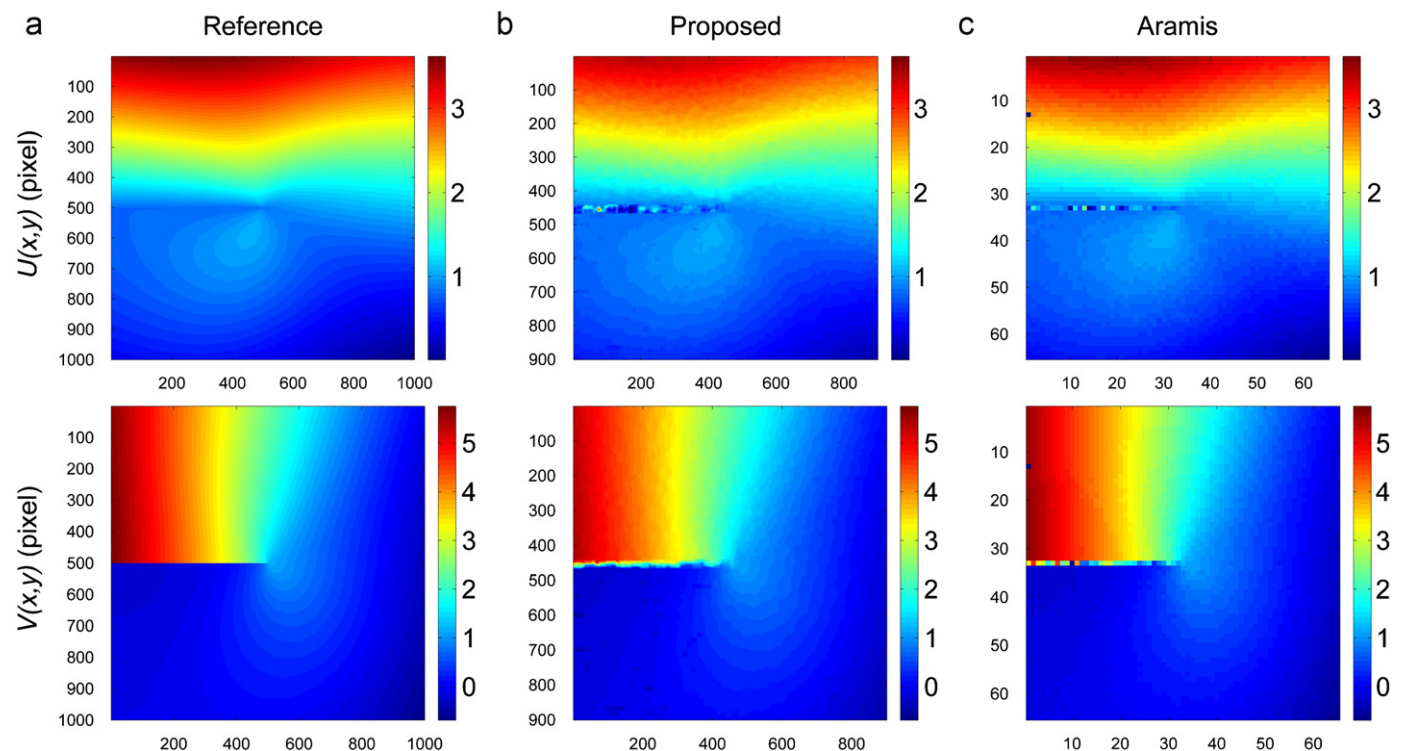


**Fig. 8.** Fracture displacement fields in mode I, including in-plane translation and rotation rigid-body movements (Fig. 1): (a) reference, (b) proposed ( $901 \times 901$  pixels) and (c) Aramis ( $65 \times 65$  subsets) DIC methods.

In order to estimate the crack tip location the same previous setup of parameters was used. The relative error obtained for both the methods with regard to the reference location is shown in Fig. 7b. The proposed method retrieves a better approximation to the expected value when compared to Aramis, with correct crack tip location for  $c=6.5$ .

The results obtained from the calculated displacements using a least-squares approach for assessing stress intensity factor  $K_I$  parameter, in-plane rigid-body translation ( $U_0$ ,  $V_0$ ) and rotation ( $\theta_U$ ,  $\theta_V$ ), are summarised in Table 2. This evaluation was performed taking separately  $U(x,y)$  and  $V(x,y)$ , as well as considering both together ( $U(x,y), V(x,y)$ ). For the proposed method, in all cases,  $K_I$  could be accurately calculated with differences less than 0.28%. This value was also determined from the displacement fields measured by the Aramis method, with low differences (less than  $-0.56\%$ ), but still higher than the proposed method. The in-plane rigid-body parameters were also retrieved accurately by both methods with errors in general less than 1%.

#### 4.3. Mode I fracture mechanical test including out-of-plane rigid-body movements

The experimental test conditions can also originate parasitic out-of-plane rigid-body displacements of the specimen, which are

a major source of errors in digital image correlation [7]. In order to quantify the influence of these parasitic displacements, a case study was carried out by coupling fracture displacement fields (Eqs. 3) with both out-of-plane translation (Eqs. 6) and rotation (Eqs. 7) movements.

The resulting displacement fields obtained by superposition of fracture (Fig. 4b) and rigid-body movements (Fig. 4e and f) are shown in Fig. 9. As it can be seen, both proposed and Aramis DIC methods qualitatively follow the reference displacement patterns.

As in the previous Sections 4.1 and 4.2, these displacement fields were further processed in order to calculate the COD<sub>I</sub> (Fig. 6c-I). The relative error obtained from both methods with regard to the reference was less than 1% (Fig. 6c-II).

The same method (Section 3.2.3) was used in order to estimate the crack tip location. The relative error obtained for both the methods with regard to the reference location is shown in Fig. 7c. Comparing both the methods, the proposed one is able to obtain the expected crack tip location with about zero error when the adequate parameter is chosen ( $c=9.5$ ). In the case of Aramis, the crack tip location is less accurate than the one obtained from the proposed method, even though an approximation can be estimated by selecting a suitable threshold parameter.

The results of the least-squares approach for assessing stress intensity factor  $K_I$  parameter, out-of-plane rigid-body translation

**Table 2**

Evaluation of mode I stress intensity factor,  $K_I$ , from displacement fields based on least-squares regression—including in-plane rigid-body movements.

		$K_I$ (MPa $\sqrt{\text{pixel}}$ )	$U_0$ (pixel)	$V_0$ (pixel)	$\theta_U$ (deg.)	$\theta_V$ (deg.)
U:	Reference	300.00	0.80	1.20	0.18	0.18
	Proposed	299.98 (−0.01%)	0.8072 (0.90%)	–	0.1812 (0.64%)	–
	Aramis	300.73 (0.24%)	0.8023 (0.29%)	–	0.1808 (0.46%)	–
V:	Proposed	299.16 (−0.28%)	–	1.1932 (−0.56%)	–	0.1790 (−0.53%)
	Aramis	298.33 (−0.56%)	–	1.1917 (−0.69%)	–	0.1797 (−0.16%)
U,V:	Proposed	299.19 (−0.27%)	0.8089 (1.11%)	1.1932 (−0.56%)	0.1812 (0.64%)	0.1790 (−0.53%)
	Aramis	298.43 (−0.52%)	0.8076 (0.95%)	1.1917 (−0.69%)	0.1808 (0.45%)	0.1797 (−0.16%)

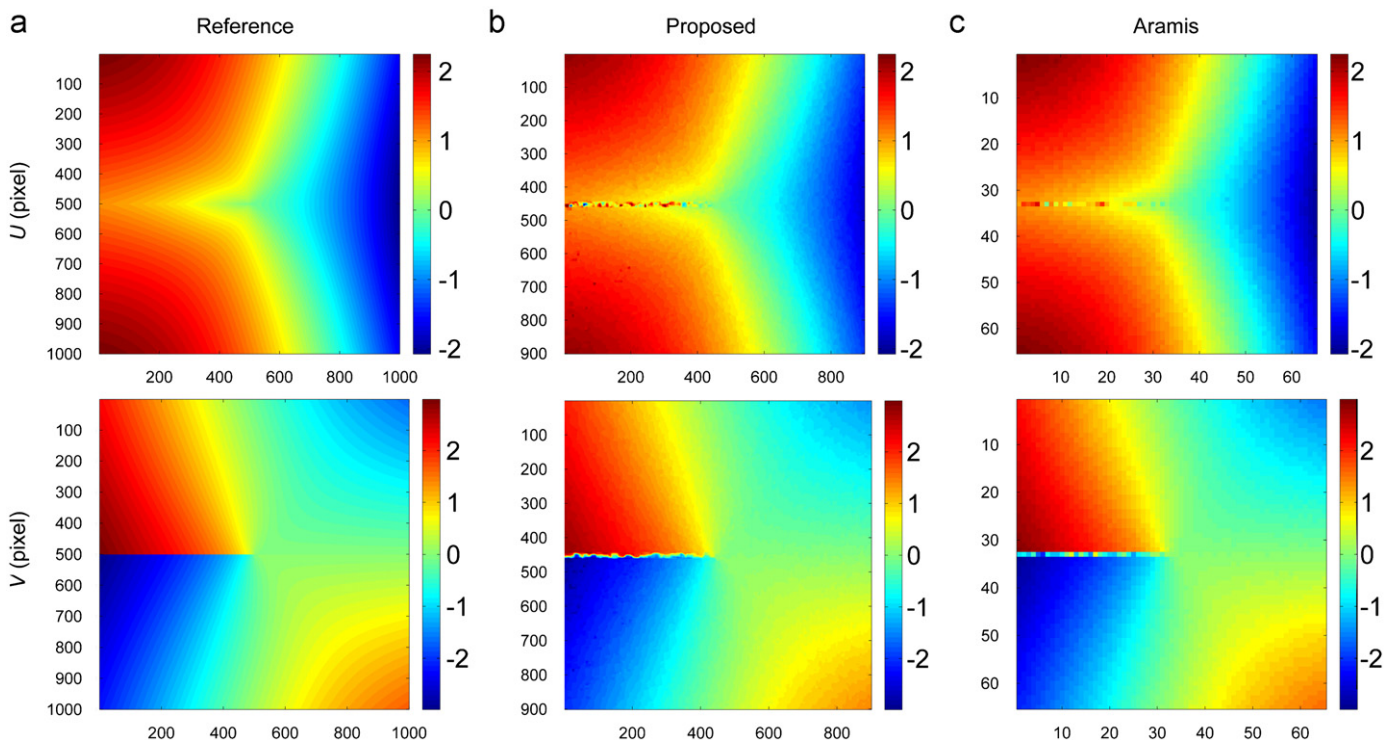


**Fig. 9.** Fracture displacement fields in mode I, including out-of-plane translation and rotation rigid-body movements (Fig. 1): (a) reference, (b) proposed (901 × 901 pixels) and (c) Aramis (65 × 65 subsets) DIC methods.

**Table 3**

Evaluation of mode I stress intensity factor,  $K_I$ , from displacement fields based on least-squares regression—including out-of-plane rigid-body movements.

		$K_I$ (MPa $\sqrt{\text{pixel}}$ )	$\Delta z$ (mm)	$\theta(\Delta z)$ (deg.)
	Reference	300	0.8	2.0
U:	Proposed	299.05 (−0.31%)	0.79935 (−0.08%)	1.9526 (−2.37%)
	Aramis	298.07 (−0.64%)	0.80033 (0.04%)	1.9612 (−1.94%)
V:	Proposed	298.91 (−0.36%)	0.79998 (−0.003%)	1.9748 (−1.26%)
	Aramis	298.50 (−0.50%)	0.80012 (0.01%)	1.9798 (−1.01%)
U,V:	Proposed	298.97 (−0.34%)	0.80019 (0.02%)	1.973 (−1.35%)
	Aramis	298.31 (−0.56%)	0.79942 (−0.07%)	1.9849 (−0.76%)

( $\Delta z$ ) and rotation ( $\theta(\Delta z)$ ) from the calculated displacements are summarised in Table 3. This evaluation was also performed taking separately  $U(x,y)$  and  $V(x,y)$  displacement fields and also considering both together ( $U(x,y), V(x,y)$ ). For the proposed method,  $K_I$  could be accurately calculated in all cases with differences less than 0.36%. When determining  $K_I$  from the displacement fields measured by the Aramis method, differences below −0.64% were obtained with regard to reference, which although small are still higher than the proposed method. The out-of-plane rigid-body parameters were also retrieved accurately but showing some sensitivity to rotations in the overall analysis, with errors slightly higher for the out-of-plane rotation parameter (−2.37%).

## 5. Conclusions

DIC method has received much attention in the last few decades because of its relatively simple principle, setup and flexibility of application. However, despite the progressive increase in pixel resolution of digital cameras, a major drawback of this technique is the subset-based feature, which imposes a compromise between accuracy and interpolation errors when defining the correlation window size. More recently, developments have been focused on novel approaches to enhance the spatial resolution of the method, in order to be able to deal with discontinuous kinematic fields.

In this work a point wise digital image correlation method combining cross-correlation and spatio-temporal differential techniques was proposed for assessing discontinuous displacement fields. The accuracy and robustness of the method were assessed on a set of numerical tests, simulating a fracture mechanical test in mode I, by processing synthetic speckled-pattern images. Effects of in-plane and out-of-plane rigid-body movements were also considered in this study, since they can occur when processing experimental data. In the analyses, the results obtained from the proposed method were systematically compared to references as well as to data obtained with GOM<sup>®</sup> Aramis v6.0.2 DIC2D commercial code. Globally, the results computed from both the methods are in good agreement with the reference values. However, due to the high spatial resolution, a better matching of the displacements in the neighbour of discontinuities could be obtained by the proposed method. These conclusions are supported by comparing both the methods with the generated reference discontinuous displacement fields, but also when assessing specific parameters namely, the crack opening displacement, the crack tip location and the stress intensity factor. This numerical validation of the proposed DIC method in the presence of discontinuous displacement fields is encouraging and will enable its application and validation, in a future work, on experimental tests. Time consuming issues might be also address with some algorithm optimizations.

## Acknowledgement

The authors thank the Portuguese Foundation for Science and Technology for supporting the work here presented, through the research Project PTDC/EME-PME/114443/2009 and the *Ciência2008* program.

## Appendix A

The stress intensity factor ( $K$ ) is a parameter characterising the fracture behaviour of solids in applications where linear elastic fracture mechanics (LEFM) holds. An analytical asymptotic displacement field can be defined as a function of  $K$ , elastic properties of the material ( $E, \nu$ ) and polar coordinates ( $r, \theta$ ) across the region of interest. In mode I, the displacement fields around the crack tip can be described as

$$U_I(r, \theta) = \frac{K_I}{2E} \sqrt{\frac{r}{2\pi}} (1 + \nu) \left[ (2k-1) \cos \frac{\theta}{2} - \cos \frac{3\theta}{2} \right] \quad (\text{A.1})$$

$$V_I(r, \theta) = \frac{K_I}{2E} \sqrt{\frac{r}{2\pi}} (1 + \nu) \left[ (2k+1) \sin \frac{\theta}{2} - \sin \frac{3\theta}{2} \right] \quad (\text{A.2})$$

Since field data is provided by digital image correlation, an overdetermined system of equations is obtained, which can be properly solved using least-squares regression.

In experimental tests the specimen can undergo not only deformation but also rigid-body displacements. Therefore, the total displacement field can be assumed as a superposition of several contributions. Let us consider fracture in mode I and out-of-plane movements, consisting of out-of-plane translation ( $\Delta z$ ) coupled with out-of-plane clockwise rotation ( $\theta$ ) about the Y axis of the image (see Section 3.2.1.3). In this case study, the measured  $U(x,y)$  component of the displacement field is given by

$$U(x,y) = \begin{bmatrix} \frac{x}{Z} & x & x \frac{x}{Z} & A_I \end{bmatrix} \begin{bmatrix} \Delta z \\ \alpha \\ \beta \\ K_I \end{bmatrix} \quad (\text{A.2})$$

where ( $X,Y$ ) are the coordinates of an imaged “point” of the object, ( $x,y$ ) are its projection point on the camera sensor (pinhole camera model),  $\alpha = \cos \theta - 1$ ,  $\beta = \sin \theta \cos \theta$  and  $A_I = \frac{1}{2E} \sqrt{\frac{r}{2\pi}} (1 + \nu) [(2k-1) \cos \frac{\theta}{2} - \cos \frac{3\theta}{2}]$ . At the same time, the measured  $V(x,y)$  component of the displacement field can be written as

$$V(x,y) = \begin{bmatrix} \frac{y}{Z} & y \frac{x}{Z} & B_I \end{bmatrix} \begin{bmatrix} \Delta z \\ \gamma \\ K_I \end{bmatrix} \quad (\text{A.3})$$

with  $\gamma = \sin \theta$  and  $B_I = \frac{1}{2E} \sqrt{\frac{r}{2\pi}} (1 + \nu) [(2k+1) \sin \frac{\theta}{2} - \sin \frac{3\theta}{2}]$ . The concept of pseudo-inverse can then be used for solving Eqs. (A.2–3) for  $K_I$  in least-square sense, thus taking into account out-of-plane rigid-body movements.

## References

- [1] Grédiac M. The use of full-field measurement methods in composite material characterisation: interest and limitations. *Composites Part A: Applied Science and Manufacturing* 2004;35(7–8):751–61.
- [2] Sutton M, Orteu J-J, Schreier H. Image correlation for shape, motion and deformation measurements: basic concepts, theory and applications. Springer; 2009.
- [3] Pan B, Qian K, Xie H, Asundi A. Two-dimensional digital image correlation for in-plane displacement and strain measurement: a review. *Measurement Science and Technology* 2009;20(6):062001.
- [4] Sutton MA, McNeill SR, Jang J, Babai M. The effects of subpixel image restoration on digital correlation error estimates. *Optical Engineering* 1988;27(10):173–5.

- [5] Bing P, Min XH, Qin XB, Long DF. Performance of sub-pixel registration algorithms in digital image correlation. *Measurement Science and Technology* 2006;17(6):1615–21.
- [6] Pan B, Li K. A fast digital image correlation method for deformation measurement. *Optics and Lasers in Engineering* 2011;49(7):841–7.
- [7] Bornert M, Brémand F, Doumalin P, Dupré J-C, Fazzini M, Grédiac M, Hild F, Mistou S, Molimard J, Orteu J-J, Robert L, Surrel Y, Vacher P, Wattrisse B. Assessment of digital image correlation measurement errors: methodology and results. *Experimental Mechanics* 2009;49(3):353–70.
- [8] Haddadi H, Belhabib S. Use of rigid-body motion for the investigation and estimation of the measurement errors related to digital image correlation technique. *Optics and Lasers in Engineering* 2008;46(2):185–96.
- [9] Sutton MA, Yan JH, Tiwari V, Schreier HW, Orteu JJ. The effect of out-of-plane motion on 2D and 3D digital image correlation measurements. *Optics and Lasers in Engineering* 2008;46(10):746–57.
- [10] Lecompte D, Smits A, Bossuyt S, Sol H, Vantomme J, Van Hemelrijck D, Habraken AM. Quality assessment of speckle patterns for digital image correlation. *Optics and Lasers in Engineering* 2006;44(11):1132–45.
- [11] Yaofeng S, Pang JHL. Study of optimal subset size in digital image correlation of speckle pattern images. *Optics and Lasers in Engineering* 2007;45(9):967–74.
- [12] Pan B, Xie H, Wang Z, Qian K, Wang Z. Study on subset size selection in digital image correlation for speckle patterns. *Optics Express* 2008;16(10):7037–48.
- [13] Triconnet K, Derrien K, Hild F, Baptiste D. Parameter choice for optimized digital image correlation. *Optics and Lasers in Engineering* 2009;47(6):728–37.
- [14] Pan B, Lu Z, Xie H. Mean intensity gradient: an effective global parameter for quality assessment of the speckle patterns used in digital image correlation. *Optics and Lasers in Engineering* 2010;48(4):469–77.
- [15] Jin H, Bruck H. Theoretical development for pointwise digital image correlation. *Optical Engineering* 2005;44(067003). 1–067003.14.
- [16] Réthoré J, Hild F, Roux S. Shear-band capturing using a multiscale extended digital image correlation technique. *Computer Methods in Applied Mechanics and Engineering* 2007;196:5016–30.
- [17] Réthoré J, Hild F, Roux S. Extended digital image correlation with crack shape optimization. *International Journal for Numerical Methods in Engineering* 2008;732:248–72. doi: 10.1002/nme.2070.
- [18] Chen J, Zhang X, Zhan N, Hu X. Deformation measurement across crack using two-step extended digital image correlation method. *Optics and Lasers in Engineering* 2010;48(11):1126–31.
- [19] Poissant J, Barthelat F, Novel A. “Subset splitting” procedure for digital image correlation on discontinuous displacement fields. *Experimental Mechanics* 2010;50(3):353–64.
- [20] Sousa AMR, Xavier J, Vaz M, Morais JLL, Filipe VMJ. Cross-correlation and differential technique combination to determine displacement fields. *Strain*. (Published online in 18/June/2010. doi: 10.1111/j.1475-1305.2010.00740.x).
- [21] Lewis JP. Fast normalized cross-correlation, in vision interface. *Canadian Image Processing and Pattern Recognition Society* 1995:120–3.
- [22] Haralick RM, Shapiro LG. *Computer and robot vision*. Addison-Wesley II; 1992. p. 316–7.
- [23] Lucas B, Kanade, T. An iterative image registration technique with an application to stereo vision. In: *Proceedings of the DARPA IU Workshop*; 1981. p. 121–30.
- [24] ARAMIS commercial software. GOM (<http://www.gom.com/>).
- [25] Gdoutos EE. *Fracture mechanics: an introduction*. 2nd ed. Springer; 2005.
- [26] Grégoire D. Initiation, propagation, arrêt et redémarrage de fissures sous impact. PhD thesis. LaMCoS-INSA de Lyon; 2008.
- [27] Catalanotti G, Camanho PP, Xavier J, Dávila CG, Marques AT. Measurement of resistance curves in the longitudinal failure of composites using digital image correlation. *Composites Science and Technology* 2010;70. 1986–199.
- [28] Nguyen TL, Hall SA, Vacher P, Viggiani G. Fracture mechanisms in soft rock: identification and quantification of evolving displacement discontinuities by extended digital image correlation. *Tectonophysics* 2011;503(1–2):117–28.
- [29] Yoneyama S, Morimoto Y, Takashi M. Automatic evaluation of mixed-mode stress intensity factors utilizing digital image correlation. *Strain* 2006;42(1). 1475–1305.
- [30] Yates J, Zanganeh M, Tai Y. Quantifying crack tip displacement fields with DIC. *Engineering Fracture Mechanics* 2010;77(11):2063–76.